



## Article

# Preflight Spectral Calibration of the Ozone Monitoring Suite-Nadir on FengYun 3F Satellite

Qian Wang<sup>1,2,3,4,5</sup>, Yongmei Wang<sup>6,7,8,9</sup>, Na Xu<sup>3,4,5,\*</sup>, Jinghua Mao<sup>6,8,9</sup>, Ling Sun<sup>3,4,5</sup>, Entao Shi<sup>6,8,9</sup>, Xiuqing Hu<sup>3,4,5</sup>, Lin Chen<sup>3,4,5</sup>, Zhongdong Yang<sup>3,4,5</sup>, Fuqi Si<sup>2</sup>, Jianguo Liu<sup>2</sup> and Peng Zhang<sup>10</sup>

- <sup>1</sup> University of Science and Technology of China, Hefei 230026, China; qw2019@mail.ustc.edu.cn
  - <sup>2</sup> Anhui Institute of Optics and Fine Mechanics, Hefei Institutes of Physical Science, Chinese Academy of Sciences, Hefei 230031, China; sifuqi@aiofm.ac.cn (F.S.); jgliu@aiofm.ac.cn (J.L.)
  - <sup>3</sup> National Satellite Meteorological Center (National Center for Space Weather), China Meteorological Administration, Beijing 100081, China; sunl@cma.gov.cn (L.S.); huxq@cma.gov.cn (X.H.); chenlin@cma.gov.cn (L.C.); yangzd@cma.gov.cn (Z.Y.)
  - <sup>4</sup> Innovation Center for FengYun Meteorological Satellite, Beijing 100081, China
  - <sup>5</sup> Key Laboratory of Radiometric Calibration and Validation for Environmental Satellites, China Meteorological Administration, Beijing 100081, China
  - <sup>6</sup> Laboratory of Space Environment Exploration, National Space Science Center, Beijing 100190, China; wym@nssc.ac.cn (Y.W.); maojinghua@nssc.ac.cn (J.M.); set@nssc.ac.cn (E.S.)
  - <sup>7</sup> School of Astronomy and Space Science, University of Chinese Academy of Sciences, Beijing 100049, China
  - <sup>8</sup> Beijing Key Laboratory of Space Environment Exploration, Beijing 100190, China
  - <sup>9</sup> Key Laboratory of Environmental Space Situation Awareness Technology, Beijing 100190, China
  - <sup>10</sup> Meteorological Observation Centre, China Meteorological Administration, Beijing 100081, China; zhangp@cma.gov.cn
- \* Correspondence: xuna@cma.gov.cn

**Abstract:** The Ozone Monitoring Suite-Nadir (OMS-N) instrument is the first hyperspectral remote sensor in the ultraviolet band of China's Fengyun series satellites. It can be used to detect several kinds of atmospheric constituents. This paper describes the prelaunch spectral calibration of the OMS-N onboard FengYun 3F. Several critical spectral parameters including the spectral resolution, spectral dispersion, and the instrument spectral response function were determined through laser-based measurements. A secondary peak of the instrument spectral response function from the short wavelength side of the ultraviolet band was found, and the possible influence on data applications was analyzed using a reference solar model and radiative transfer model. The results indicate that the spectral resolution and spectral accuracy of OMS-N meet the mission requirements. However, the asymmetries in the instrument spectral response function in the ultraviolet band were found near nadir rows, which are expressed as the "asymmetric central peak" and "secondary peak". The analysis results show that if the influences of the instrument spectral response function "asymmetric central peak" and "secondary peak" in the ultraviolet band are ignored, they will bring an error as large as 5% at the center of the absorption line.

**Keywords:** FengYun-3F; OMS-N; ultraviolet; spectral calibration



**Citation:** Wang, Q.; Wang, Y.; Xu, N.; Mao, J.; Sun, L.; Shi, E.; Hu, X.; Chen, L.; Yang, Z.; Si, F.; et al. Preflight Spectral Calibration of the Ozone Monitoring Suite-Nadir on FengYun 3F Satellite. *Remote Sens.* **2024**, *16*, 1538. <https://doi.org/10.3390/rs16091538>

Academic Editor: Manuel Antón

Received: 28 February 2024

Revised: 20 April 2024

Accepted: 24 April 2024

Published: 26 April 2024



**Copyright:** © 2024 by the authors. Licensee MDPI, Basel, Switzerland. This article is an open access article distributed under the terms and conditions of the Creative Commons Attribution (CC BY) license (<https://creativecommons.org/licenses/by/4.0/>).

## 1. Introduction

Fengyun-3F (FY-3F) is China's second-generation polar-orbiting meteorological satellite. It was launched in August 2023. The Ozone Monitoring Suite-Nadir instrument (OMS-N) onboard FY-3F is a new sensor in the FY-3 series satellites, which is mainly used to determine information on the column of atmospheric ozone (O<sub>3</sub>), sulfur dioxide (SO<sub>2</sub>), nitrogen dioxide (NO<sub>2</sub>), and other trace gases, as well as the profile of atmospheric ozone on a global scale, providing important support for climate change, atmospheric chemistry, and ozone monitoring [1,2].

Space-based instrument measures ultraviolet and ultraviolet-visible radiation backscattered by Earth's atmosphere and surface to retrieve criteria pollutants, such as O<sub>3</sub>, SO<sub>2</sub>, NO<sub>2</sub>, and aerosols. At present, several instruments including Global Ozone Monitoring Experiment 2 (GOME-2), Ozone Mapping and Profiler Suite (OMPS), TROPospheric Monitoring Instrument (TROPOMI), environmental trace gas monitoring instrument (EMI), and OMS-N are currently in operation [3–7]. These instruments cover the spectral range of ultraviolet and visible, with a spectral resolution of about 0.2–1.0 nm. The total column of O<sub>3</sub>, SO<sub>2</sub>, NO<sub>2</sub>, and the profile of the O<sub>3</sub> mixing ratio can be determined by the differential optical absorption spectroscopy (DOAS) retrieval algorithm and direct fitting algorithm, respectively [8–13]. Both algorithms rely on the knowledge of the dispersion relation and accurate knowledge of the instrument spectral response function (ISRF) [14,15]. Therefore, a thorough understanding of the OMS-N wavelength and the ISRF is critical to accurately simulating the OMS-N spectra and retrieving atmospheric constituents.

This work presents the prelaunch spectral calibration of OMS-N, which was performed in a thermal vacuum chamber. The spectral parameters of the OMS-N instrument, including the ISRF and wavelength, were carefully tested. Then, issues derived from ISRF spectral calibration were analyzed. This paper is organized as follows. Section 2 gives a brief introduction to the OMS-N instrument. Section 3 describes the method used to derive the ISRF and dispersion parameter, including the equipment and data processing method. Section 4 provides the spectral calibration and verification results, followed by an investigation of ISRF characterization on solar irradiance and earth radiance. The last section summarizes this work and offers some conclusions.

## 2. OMS-N Overview

The FY-3F OMS-N instrument observes the solar radiation reflected by the Earth and scattered by the atmosphere through a push broom observation mode, with spectra ranging from ultraviolet to visible at 250–493 nm. Spatially, OMS-N has a high spatial resolution of 7 km × 7 km for the nadir point and a wide 112° field of view, operating on an orbit altitude of 836 km to provide a global daily measurement. Figure 1 shows a schematic diagram of the OMS-N earth observation mode.

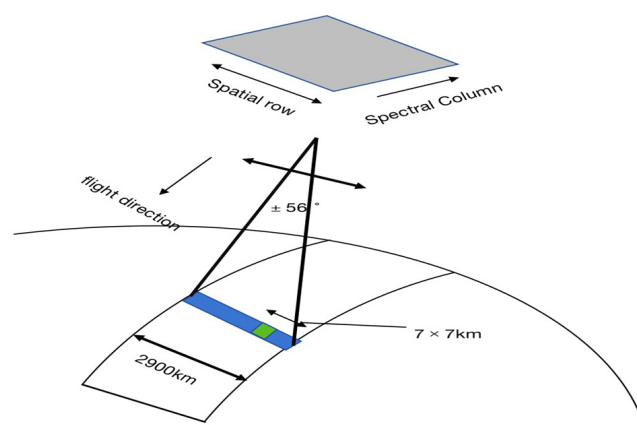


**Figure 1.** Observation schematic view of the FY-3F OMS-N instrument.

The OMS-N instrument incorporates two imaging grating spectrometers for ultraviolet (UV) and visible (VIS) spectral bands, where the UV and VIS bands cover 250–320 nm and 310–493 nm, respectively. OMS-N UV measurements are divided into the UV1 band (250–300 nm) and UV2 band (300–320 nm). In each spectrometer's focal plane, a 1024 × 1024 pixel imaging array is used to collect spatial information along the slit in one dimension and spectral information in the other dimension. The edge regions of the CCD are designed for shielding masks to acquire dark current. The main characteristics and mission requirements from the China Meteorological Administration (CMA) of the OMS-N instrument are shown in Table 1.

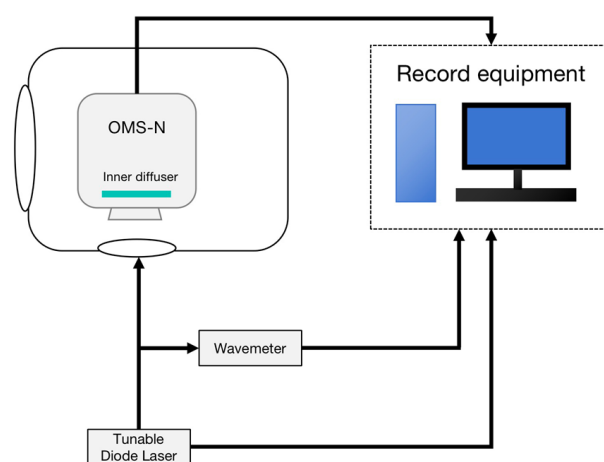
**Table 1.** The main characteristics and mission requirements of FY-3F OMS-N.

Parameter	UV1	UV2	VIS
Band coverage	250–300 nm	300–320 nm	310–497 nm
Spectral resolution	~1 nm	~0.5 nm	~0.5 nm
Spectral sampling		~0.073 nm	~0.197 nm
Spectral accuracy		0.05 nm	0.01 nm
Spatial resolution for nadir point	21 km × 28 km	7 km × 7 km	7 km × 7 km
Equator crossing time		10:00 local solar time	
Field of view		112°	

To enhance the signal-to-noise ratio, sets of 16 pixels averaged to yield 58 spatial rows in the UV1 band, and four pixels averaged to acquire 238 spatial rows in the UV2 and VIS bands, respectively. Meanwhile, the thermal control system strictly controls the detector temperature at  $-36\text{ }^{\circ}\text{C}$ , with a temperature accuracy of 0.05 K, to ensure the performance stability of the instrument.

### 3. Spectral Calibration Methodology

The spectral calibration of the OMS-N instrument includes the ISRF characterization and dispersion coefficient [16]. The ISRF displays the relative response of each detector pixel on focal plane arrays to monochromatic illumination. The dispersion coefficient describes the relationship between wavelength centroid and spectral pixel index. The common equipment used for spectral calibration is a standard spectral lamp, slit function measurement [17], and tunable laser. Standard spectral lamps can emit a limited number of spectra with high spectral accuracy and high spectral resolution on certain wavelengths. However, the wavelength of the rest of the spectral pixels needs to be calculated by interpolation or extrapolation, which may introduce uncertainties in spectral calibration. The slit function measurement determines the ISRF accurately, but it is very time-consuming to acquire the ISRF for each pixel because OMS-N ISRFs vary in both spectral and spatial dimensions of two large array detectors. Additionally, the ISRF and spectral dispersion can be determined using scanning measurements obtained with a tunable diode laser, which is widely used in spectral calibration because of its high precision [7,18–20]. OMS-N also adopts this method. However, the biggest challenge for the OMS-N instrument spectral calibration is determining the ISRF of each pixel due to the large field of view and wide spectral coverage. Therefore, the spectral calibration for OMS-N is innovatively performed by combining the tunable laser with the inner solar diffuser plate of OMS-N, scattering the monochromatic illumination from the laser to the whole spatial pixels, thus completing the spectral calibration of the OMS-N instrument for the whole field of view all at once. The test setup and schematic diagram of OMS-N spectral calibration are presented in Figure 2.

**Figure 2.** Schematic diagram of OMS-N spectral calibration.

### 3.1. Method

The spectral calibration of the OMS-N instrument is performed in a thermal vacuum chamber, with the pressure of the test environment better than  $6.65 \times 10^{-3}$  Pa. The working temperature of the spectrometer and the detector are around  $20 \text{ }^\circ\text{C} \pm 2 \text{ }^\circ\text{C}$  and  $-36 \text{ }^\circ\text{C}$ , respectively. The spectral calibration equipment of OMS-N includes a tunable diode laser manufactured by M-squared, an optical parametric oscillator (OPO) laser, and a standard spectral lamp. The tunable laser manufactured by M-squared is the major equipment, but its spectral range cannot cover 300–350 nm; thus, the OPO tunable laser is used as a supplement. The major tunable laser scans the spectra and records the measurements automatically, which largely improves efficiency. To ensure sufficient measurements within a spectral resolution, the wavelength step size of sampling is set to 0.05 nm and 0.02 nm, which is nearly 1/20~1/10 of the spectral resolution for the UV1 and VIS band, respectively. The standard spectral lamp is mainly used to verify spectral accuracy. The equipment spectral parameters and step size of sampling in calibration are shown in Table 2.

**Table 2.** The equipment spectral parameters and step size of sampling for spectral calibration.

Device	Wavelength Accuracy	Band Coverage	Sampling Step Size
M-squared tunable laser	0.001 nm	250–300 nm 350–493 nm	0.05 nm 0.02 nm
OPO tunable laser	0.0001 nm	300–350 nm	2 nm
Standard spectral lamp	0.0005 nm	253.652 nm 334.1484 nm 404.657 nm 407.7837 nm 435.834 nm	-

### 3.2. Data Processing

The characterization of the ISRF was determined using laser scanning. To eliminate random noise, 20 measurements were averaged. Thus, the OMS-N ISRF can be generated after processing including measurements averaged in spatial dimension, dark background correction, ISRF normalization, and ISRF interpolation to regular grids. The dispersion coefficients can be acquired by polynomial fitting, and then, Full Width at Half Maximum (FWHM) could also be calculated. Figure 3 presents a flowchart of the data processing procedure for spectral calibration. The spectral parameters for each pixel can be generated by repeating the procedure.

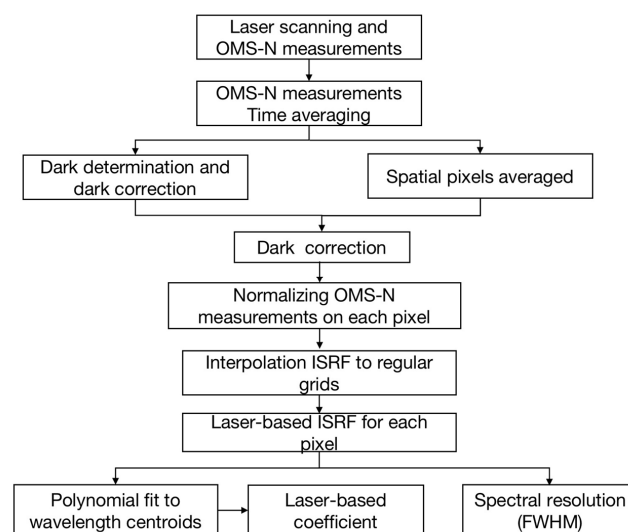


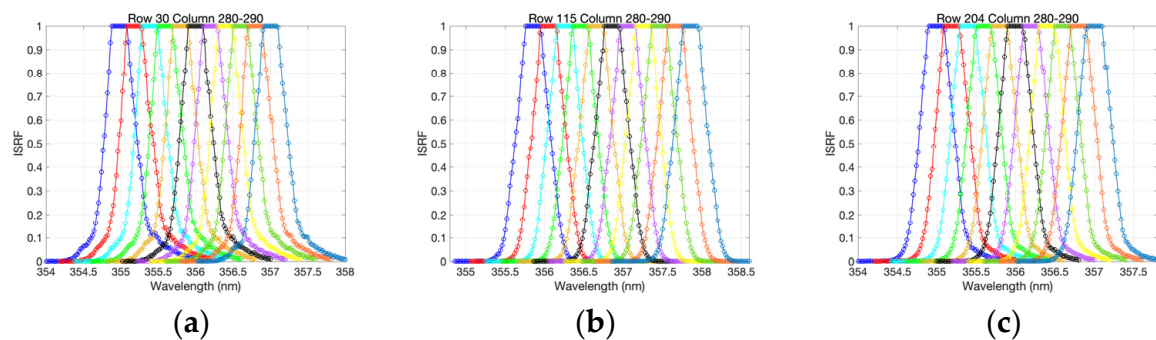
**Figure 3.** Flowchart of the data processing procedure of OMS-N spectral calibration.

## 4. Results and Discussion

### 4.1. ISRF

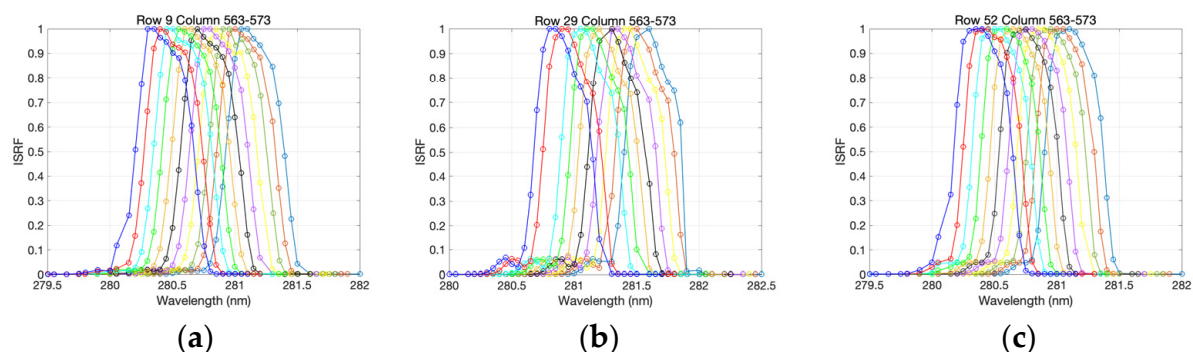
For the grating hyperspectral instrument of OMS-N, the ISRF relates to slit width, detector image spacing, optical aberrations, diffraction, detector crosstalk, stray light, etc. [18]. The ISRF is a core spectral parameter of hyperspectral instruments. The shape and consistency of the ISRF are both key parameters, indicating spectral calibration accuracy [21,22].

The detailed characterization of the ISRF at the VIS band is finely scanned by a tunable laser with a step size of 0.02 nm. Figure 4 shows the ISRF of eleven spectral pixels in the VIS band for three spatial rows. The 11 spectral ISRFs, with the highest response to certain laser scans, are displayed in different colors. It can be seen that, for a given spatial row, the ISRF varies smoothly across the spectral region. The detailed characterization of ISRFs acquired is attributed to the 25 samplings within a spectral resolution while laser scanning.



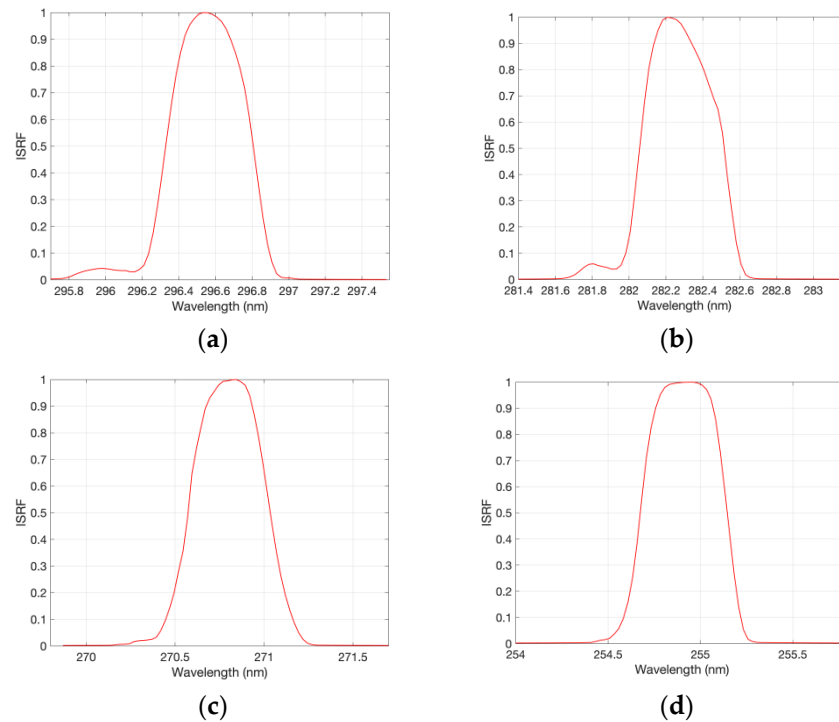
**Figure 4.** Response from a set of 11 spectral pixels (different colors) in the VIS band. (a) Row 30; (b) row 115; (c) row 204.

For the UV band, laser scans with a step size of 0.05 nm were used, such that there were  $\sim 10$  laser scans per spectral resolution. The signal from a set of 11 spectral pixels is displayed in Figure 5. The measurement for the UV1 ISRF has relatively few samplings compared with the VIS band, but the ISRF of neighboring spectral pixels remains consistent (Figure 5). In addition, it was found that the ISRF of the UV1 band displays an asymmetric central peak at row 9 and row 29 and a secondary peak from the short wavelength side at row 29 and row 52, where row 29 is the nadir row, resulting from the aberrations, which are produced by coma aberrations and multiple reflections from the optical system after the light entering the three-dimensional slit of OMS-N. Both of the characterizations are more pronounced for nadir rows and gradually diminish from nadir to side rows.



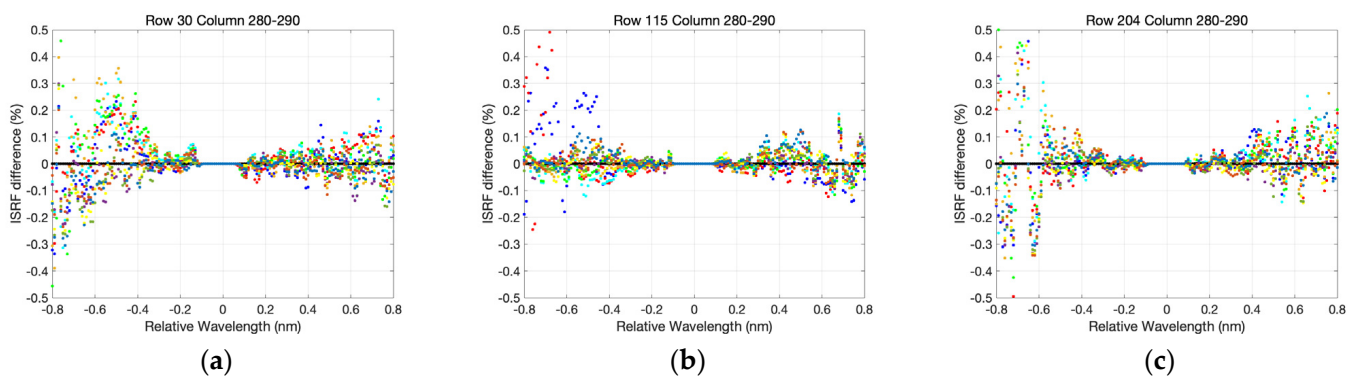
**Figure 5.** Response from a set of 11 spectral pixels (different colors) in the UV1 band. (a) Row 9; (b) row 29 (the nadir row); (c) row 52.

Figure 6 exhibits the representative ISRFs in different spectral pixels for nadir rows. It was found that the “asymmetric central peak” and “secondary peak” appearing close to 300 nm are nearly absent in the short wavelength of the UV1 band.

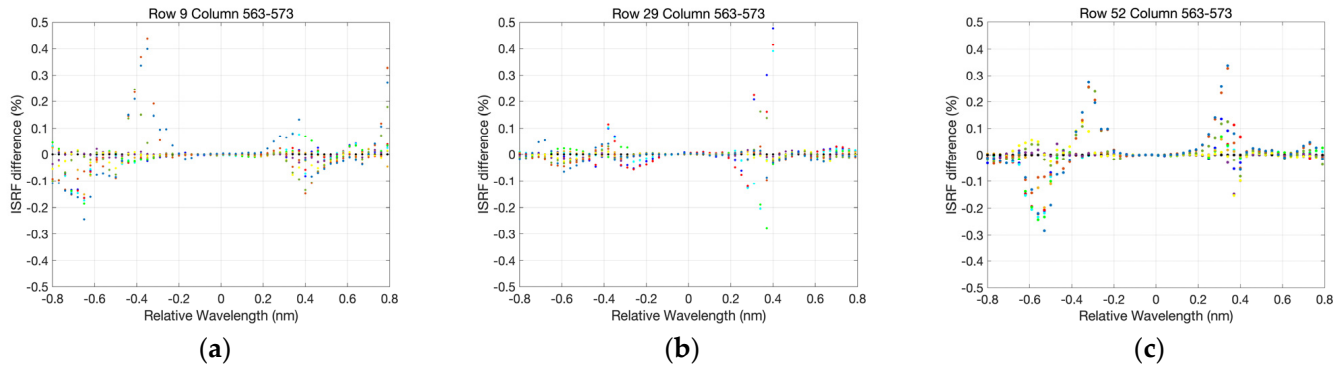


**Figure 6.** The “asymmetric central peak” and “secondary peak” characterization of the ISRF for the nadir row in the UV1 band. (a) Wavelength centroid around 296.6 nm; (b) wavelength centroid around 282.3 nm; (c) wavelength centroid around 270.8 nm; (d) wavelength centroid around 254.9 nm.

In addition, in order to assess the consistency of the ISRF, we take the central column as a reference to calculate the relative difference between the central column and others. The relative wavelength was obtained by subtracting the center wavelength of each pixel. The results of the center and side rows in the UV1 and VIS bands are shown in Figures 7 and 8. It was found that the bias gradually becomes larger from the center to the wings. The ISRF difference is negligible around the center for both the UV1 and VIS bands. For the VIS band, the bias is almost less than 0.1% within the relative wavelength of  $\pm 0.4$  nm, which is lower in row 115 than that of rows 30 and 204, especially for the long wavelength side. For the UV1 band, the samples are much smaller than the VIS band due to the limited laser scans. The bias increases at relative wavelengths around 0.4 nm, mainly due to the effect of the “asymmetric central peak” and “secondary peak” in the ISRF. The ISRF difference among neighboring pixels is less than 0.3% in most cases. Overall, the ISRF among neighboring pixels has a good consistency for both the UV and VIS bands.

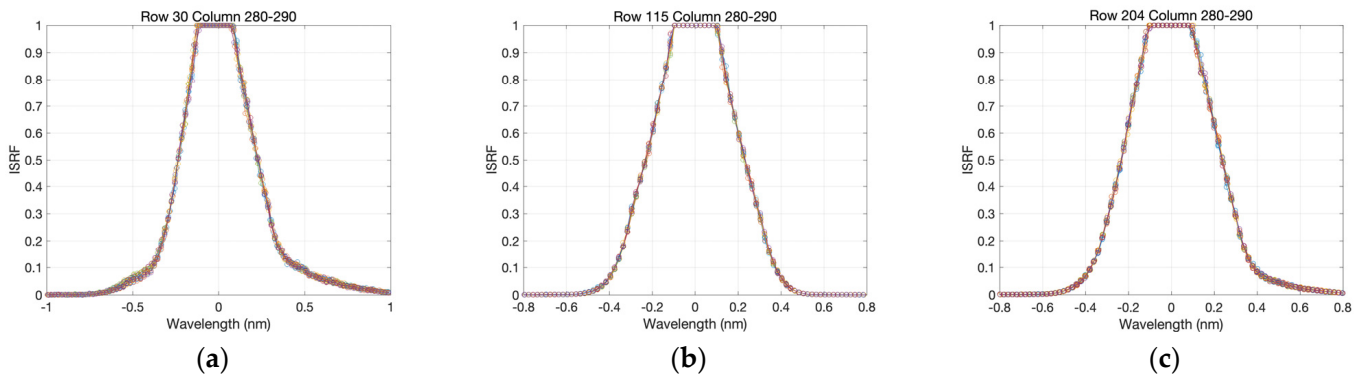


**Figure 7.** The ISRF difference in the VIS band between the center (column 285) and the others (columns 280–290). The different dots donate the ISRF differences in different columns. (a) Row 30; (b) row 115; (c) row 204.



**Figure 8.** The ISRF difference in the UV1 band between the center (column 568) and the others (columns 563–573). The different dots donate the ISRF differences in different columns. (a) Row 9; (b) row 29; (c) row 52.

Based on the fact that the ISRFs of neighboring spectral pixels are in good agreement for both the UV1 and VIS bands, the ISRF data of several adjacent pixels are combined by subtracting the center wavelength ( $\lambda_{cen}$ ) of each pixel, giving a single set of data with a much higher resolution. This helps to improve the spectral sampling of the ISRF and to accurately determine the wavelength centroid of each spectral pixel. This step can be seen in Figures 4 and 9 for the VIS band. The combined ISRF (shown in Figure 9) shows the centered response of each spectral pixel to the laser scan as a function of  $\delta\lambda = \lambda - \lambda_{cen}$ , which could reduce the influence of outliers and increase the fitting accuracy of the ISRF.



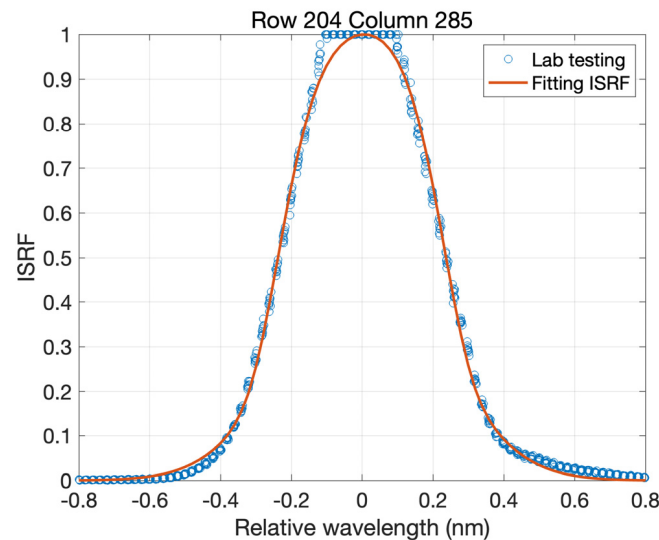
**Figure 9.** Samples from 11 spectral pixels in the VIS band are combined to give a single set of data, with a higher resolution shown by the colored circles. (a) Row 30; (b) row 119; (c) row 204.

Figure 9 illustrates the combined ISRF of 280–290 spectral pixels in the VIS band for the side and nadir spatial rows. It is concluded that the ISRFs are generally consistent in neighboring spectral pixels for different spatial rows. The ISRF exhibits a flat top in the central peaks. In the VIS band, the ISRF for the nadir row has good symmetry, whereas there is a slight asymmetry in the ISRF at the side rows. To determine the wavelength centroid with greater accuracy, the linear combination of a Gaussian and flat-top Gaussian is used based on the combined ISRF, as shown in Equation (1) as follows:

$$S = \omega e^{-\frac{(x-a_1)^2}{2c_1^2}} + (1-\omega)e^{-\frac{(x-a_2)^4}{2c_2^4}} \quad (1)$$

where  $\omega$  is the relative weighting between the standard and flat-top Gaussian.  $c_1$  and  $c_2$  are half-width at 1/e for standard and flat-top Gaussian.  $a_1$  and  $a_2$  are their centroid wavelengths. These five parameters are fitted simultaneously using Equation (1) by a non-linear least square fitting method. Note that  $a_1$  and  $a_2$  can be different, resulting in an asymmetric ISRF.

According to Equation (1), the ISRF of the central pixel was obtained by nine adjacent pixel samplings in the VIS band. Figure 10 shows combined spectral sample data and the fitted ISRF for a certain pixel. Note that, in order to obtain the combined ISRF shown in Figure 10, the initial  $\lambda_{cen}$  was determined from a Gaussian fit to acquire the center of each ISRF. Then, once the combined ISRF is acquired, the optimized wavelength centroid and spectral resolution can be obtained.



**Figure 10.** Combined ISRF spectral sample data (blue circle) and the fitted ISRF (red line) at row 204, column 285 in the VIS band.

For the UV1 band, it can be seen in Figure 11 that the ISRFs are also almost the same for the neighboring spectral pixels. The flat-top Gaussian function shown in Equation (2) is used to fit the ISRF by five combined spectral sample data.

$$S = e^{-\frac{(x-a)^4}{2c^4}} \quad (2)$$

where  $c$  is half-width at  $1/e$  for flat-top Gaussian and  $a$  is the Gaussian centroid wavelength.

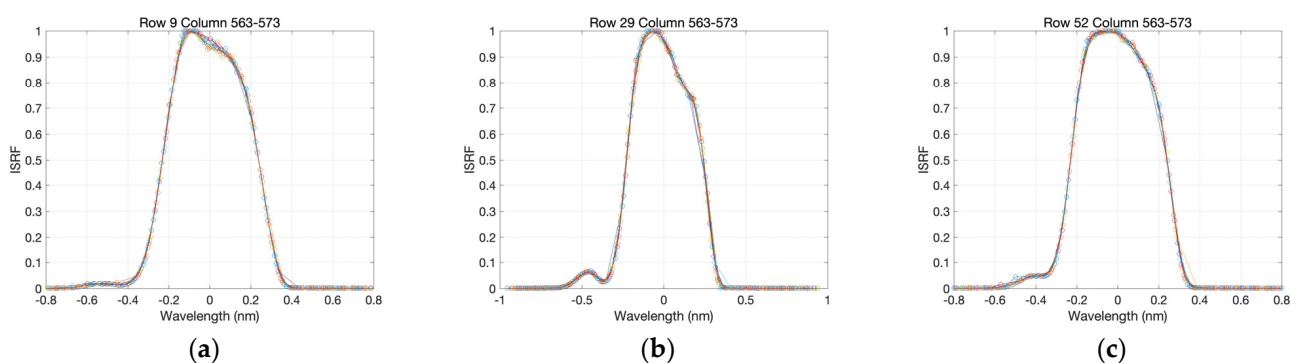


**Figure 11.** Samples from 11 spectral pixels in the UV1 band are combined to give a single set of data, with a higher resolution shown by the colored circles. (a) Row 9; (b) row 29; (c) row 52.

As displayed in Figure 12, although the flat-top Gaussian function cannot fit the ISRF characterizations—the “asymmetric central peak” and “secondary peak”—well, the fitted ISRF profile is in good agreement with the spectral sampling. Figure 12 shows the worst case of the ISRF affected by the “asymmetric central peak” and “secondary peak”. Most of the ISRFs are far better than the example shown in Figure 12, especially for the short wavelength of the UV1 band; ISRFs are very close to flat-top Gaussian.

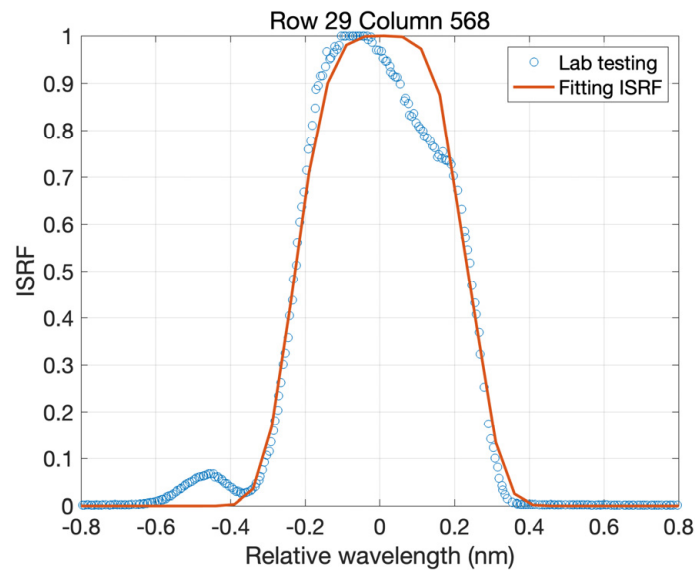


**Figure 12.** Combined ISRF spectral sample data (blue circle) and the fitted ISRF (red line) at row 29, column 568 in the UV1 band.

Further, we use the goodness of fit and root-mean-square error (RMSE) to assess how well the measured ISRF aligns with the fitted ISRF. For a given pixel, the combined ISRF and fitted ISRF points can be expressed as  $[(x_1, y_1), (x_2, y_2) \dots (x_k, y_k)]$  and  $[(x_1, \hat{y}_1), (x_2, \hat{y}_2) \dots (x_k, \hat{y}_k)]$ , respectively. The goodness of fit and RMSE can be calculated using Equations (3)–(5) and Equation (6), respectively.

$$R_{adjusted}^2 = 1 - \left( \frac{n-1}{dfe} \right) \frac{SSE}{SST} \quad (3)$$

$$SST = \sum_{k=1}^n (y_i - \bar{y})^2 \quad (4)$$

$$SSE = \sum_{k=1}^n (\hat{y}_i - y_i)^2 \quad (5)$$

$$rmse = \sqrt{\frac{1}{n} \sum_{i=1}^n (y_i - \hat{y}_i)^2} \quad (6)$$

where  $n$  is the number of sample points from the combined ISRF.  $dfe$  is the degree of freedom.  $\bar{y}$  is the mean of the response variable  $y_i$ ,  $y_i$ , and  $\hat{y}_i$  are the sample points in the combined ISRF and the fitted ISRF. SST is the sum of squared differences between individual measured points ( $y_i$ ) and the mean of the response variable ( $\bar{y}$ ). SSE is the sum of squared differences between fitted data ( $\hat{y}_i$ ) and measured data points ( $y_i$ ). The better goodness of fit depends on the smaller SSE.

For the VIS band, the maximum ISRF differences between the measured and fitted points are within 0.1, corresponding to the relative wavelength region of  $(-0.2, -0.05)$  and  $(0.05, 0.2)$ . For other points, the differences between these two are much smaller than 0.1 and generally close to 0, as shown in Figure 10. Statistical analyses showed that the average goodness of fit for all pixels was 0.997, with a root-mean-square error of 0.026.

For the UV1 band, it can be found in Figure 12 that the maximum distance between  $\hat{y}_i$  and  $y_i$  seems larger in some pixels affected by the “asymmetric central peak” and “secondary peak”. But most of the pixels are much better than that. Therefore, the statistical analysis results of all UV1 pixels show that the averaged goodness of fit in the UV1 band is 0.994, with a root-mean-square error of 0.024. In this case, it is possible to accurately calculate the spectral resolution. Considering the asymmetric ISRF in some pixels, the wavelength centroid is calculated using a barycenter instead of a Gaussian center for the UV1 band.

Note that, for the spectral range of 300–350 nm in the UV2 and VIS bands, the ISRF of some spectral pixels was performed using an OPO laser combined with a wavemeter to ensure the accuracy of the spectral calibration at the edge of band coverage. The ISRF for 300–350 nm was obtained according to Equation (1). Additionally, the ISRF for each pixel will be provided to the users. The ISRF for the UV1 and VIS bands derives from the spectral calibration test, and the measured ISRF will be provided. For the UV2 band, the ISRF fitting function and coefficients will be shared. Figure 13 displays an example of the UV2 ISRF.

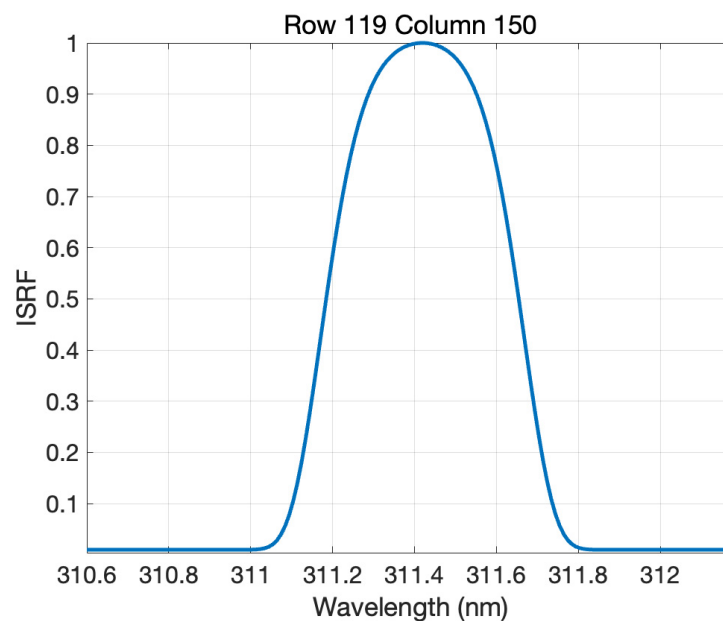


**Figure 13.** The ISRF in the UV2 band for row 119, column 150.

#### 4.2. Spectral Dispersion

The core purpose of the spectral calibration is to establish the mapping between spectral pixel index and wavelength. Based on the combined ISRF sampling data, the wavelength centroid of each pixel in the VIS and UV2 bands was calculated using a Gaussian-family fitting function. For the UV1 band, the barycenter of the ISRF was used to determine the wavelength centroid. The calibration equations for the spectral pixel index and wavelength were established.

The fitting residuals of the spectral dispersion coefficients were calculated for each spatial row. The residual was calculated according to Equation (7) as follows:

$$residual(i) = \sqrt{\sum(\lambda(i,j) - \lambda_{center}(i,j))^2 / (n - 1)} \quad (7)$$

where  $i$  and  $j$  are the index of the spatial row and spectral column.  $\lambda$  is the wavelength calculated by dispersion coefficients.  $\lambda_{center}$  is calculated from the combined ISRF.  $n$  is the total number of spectral pixels.

The residuals of the polynomial fit to wavelength centroids and spectral dispersion are shown in Figure 14. The fit residuals decrease with the order of the polynomial varying from second order to fifth order. The fifth-order fit residuals in the UV1 and VIS bands are better than 0.025 nm and 0.012 nm. For the UV2 band, the residuals seem much smaller than that of the UV1 and VIS bands. The small residuals may be due to the limited samples in the UV2 band, so the results may not be sufficiently representative. The sharp increase in residuals in the VIS band is due to the spatial rows beyond the valid range. In the end, a fifth-order polynomial was sufficient to model the spectral dispersion in the UV1, UV2, and VIS bands. Additionally, it was shown in Figure 15 that the pixel centroid wavelengths of a given spatial row varied smoothly across the band for the UV1, UV2, and VIS bands.

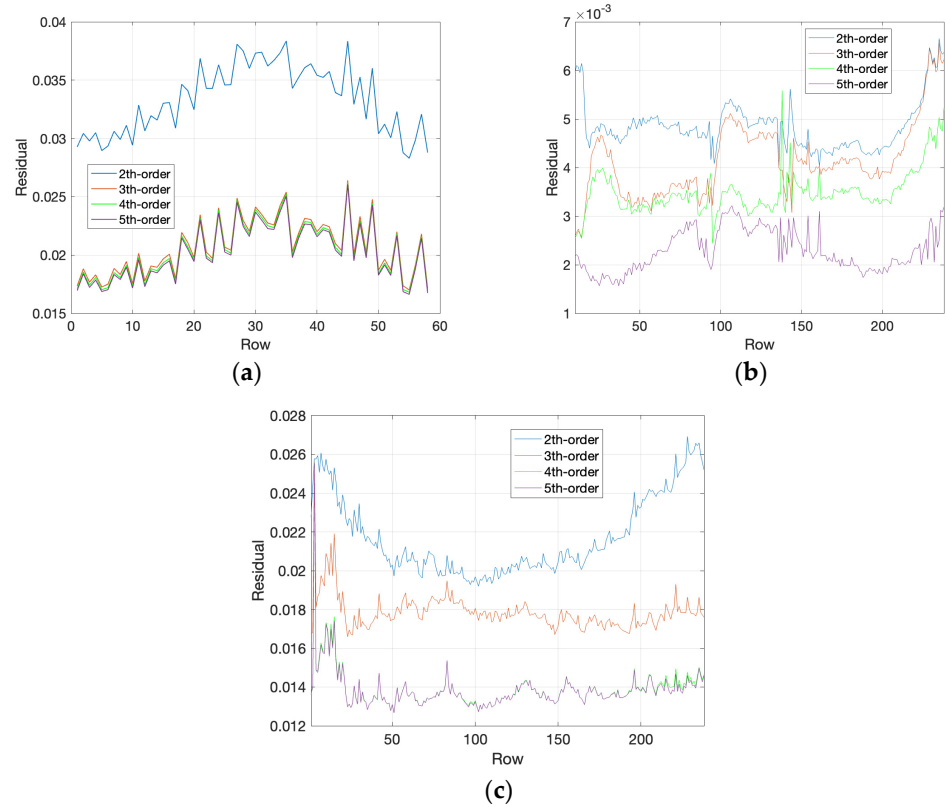


**Figure 14.** Polynomial fits residuals of the spectral dispersion coefficients of second order (blue), third order (red), fourth order (yellow), and fifth order (purple). (a) UV1 band; (b) UV2 band; (c) VIS band.

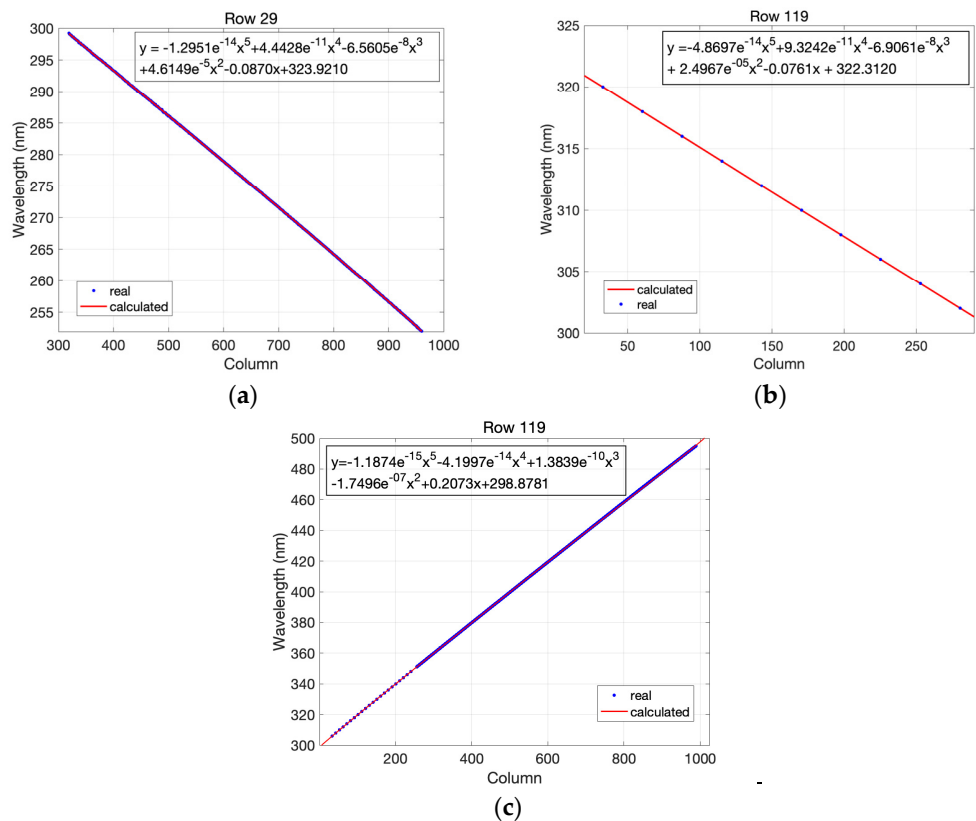


**Figure 15.** Fifth-order polynomial fits (red line) for nadir row wavelength centroids derived from (blue dots) laser data as a function of the spectral pixel index. (a) UV1 band; (b) UV2 band; (c) VIS band.

#### 4.3. Spectral Resolution

Spectral resolution is a key spectral parameter to access the spectral characterization of hyperspectral instruments. In this study, spectral resolution is defined as the FWHM of the ISRF. The spectral resolution of OMS-N was calculated using the fitted ISRF. The results show that the FWHM of the UV1, UV2, and VIS bands are in the range of 0.52–0.563 nm, 0.4–0.45 nm, and 0.4–0.5 nm, respectively. Additionally, the spectral resolving power ( $\frac{\lambda}{\delta\lambda}$ ) of the three bands are ~540, 600, and 666, respectively, where  $\lambda$  and  $\delta\lambda$  denote the wavelength and the spectral resolution [23,24]. The spectral resolutions of OMS-N satisfy the mission requirements shown in Table 1.

#### 4.4. Verification of Wavelength Accuracy

Verification of spectral accuracy was made by a standard spectral lamp. Figure 16 shows the OMS-N digital number (DN) response to the standard spectral lamp in the UV and VIS bands. To avoid the effect of spectral overlap, one reference wavelength was selected in the UV1 band and four were selected in the VIS band to verify OMS-N spectral accuracy.

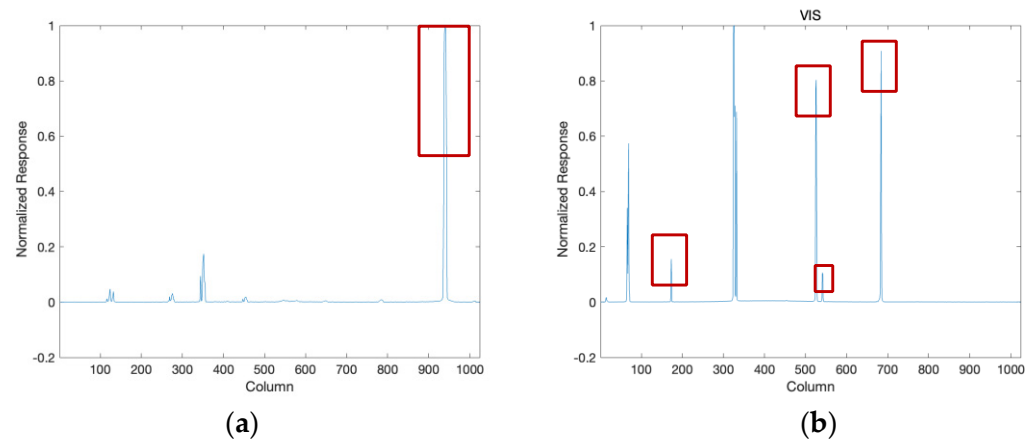


**Figure 16.** OMS-N response to the standard spectral lamp, and the red rectangle shows the selected standard spectral line. (a) UV band; (b) VIS band.

The verification results of wavelength accuracy based on the standard spectral lamp are shown in Table 3. The spectral accuracy in the UV1 and VIS bands meet the OMS-N preflight wavelength calibration requirement shown in Table 3. It should be noted that this analysis did not include the UV2 band due to the absence of a standard spectral line at 300–320 nm. Verification for the UV2 band needs to be performed using on-orbit solar observations.

**Table 3.** The wavelength accuracy of OMS-N at the reference wavelength.

Band	Reference Wavelength (nm)	Wavelength Accuracy (nm)	Requirement (nm)
UV1	253.652	−0.031	0.05
VIS	334.1484	−0.010	0.01
	404.657	−0.0014	
	407.7837	0.0058	
	435.834	−0.0061	

#### 4.5. Analysis of the ISRF in the UV1 Band

Observed spectra can be simulated as a convolution of the ISRF and the high-resolution reference spectra. A thorough understanding of the ISRF is crucial to accurately simulate the spectra and retrieve atmospheric constituents. Given the “asymmetric central peak”

and “secondary peak” of the ISRF for OMS-N in the UV1 band, the probable influences on solar irradiance and the Earth’s radiance were analyzed.

#### 4.5.1. The “Secondary Peak” of the ISRF in the UV1 Band

As shown in Section 4.1, the “secondary peak” can be seen in some pixels of the UV1 band. To understand the influence of the “secondary peak” and its significance, the response ratio in the “secondary peak” and the whole spectral domain was calculated. The response ratio indicates the radiometric contribution from the “secondary peak”, which could affect the radiometric energy concentration degree of a pixel. The response ratio can be defined as follows:

$$R(i, j) = I_s(i, j) / I_w(i, j) \times 100\% \quad (8)$$

where  $i$  and  $j$  denote the spatial row and spectral column.  $I_s$  and  $I_w$  are the response in the “secondary peak” and the whole spectral domain in a certain pixel.  $R$  denotes the response proportion introduced by the “secondary peak”.

The analysis was performed for all the pixels related to the “secondary peak” in the UV1 band. The results in Figure 17 indicate that the radiometric response from the “secondary peak” is about 1.6% for most of the related pixels, but the maximum can reach 3.5%. Accordingly, the impact of the “secondary peak” needs to be further discussed.

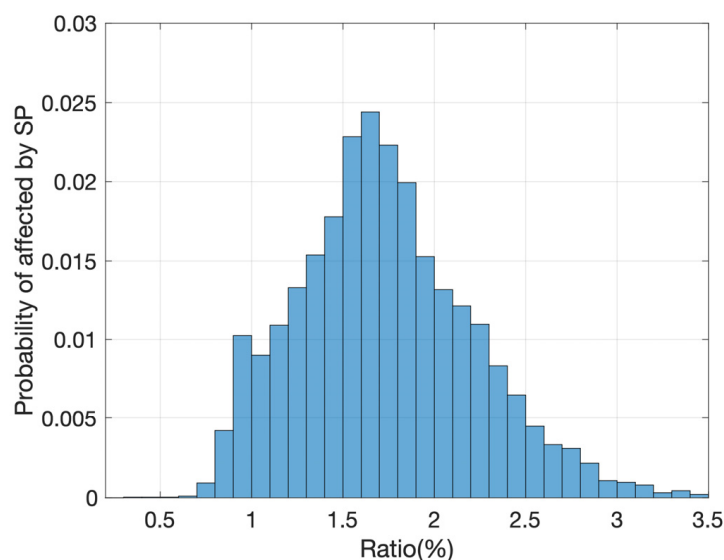


**Figure 17.** Histogram of the response ratio distribution of the ISRF “secondary peak” for all affected pixels in the UV1 band.

#### 4.5.2. Impact Analysis: Reference Solar Spectra

Solar irradiance spectra are significant for OMS-N on-orbit calibration and atmospheric constituent retrieval. The ISRF directly relates to simulated solar irradiance through convolution. In this section, to discuss the probable influence of the UV1 ISRF on simulated solar irradiance spectra, an attempt is made using the high-accuracy Total and Spectral Solar Irradiance Sensor (TSIS) reference solar spectra [25] and the testing ISRF.

As discussed in Section 4.1, the ISRF of OMS-N exhibits different characterizations in UV1 wavelength coverage. The ISRF in the middle wavelength mainly displays the characterization of the “asymmetric central peak” and “secondary peak”, while the ISRF in the long wavelength shows a “secondary peak” and a much smaller “asymmetric central peak”, and then the ISRF in the short wavelength is almost absent of the above characterizations. The potential uncertainty of the ISRF characterizations was evaluated using the above representative OMS-N measured and the testing ISRF in UV1 shown in Figure 18. The testing ISRF was fitted by a flat-top Gaussian function using the FWHM from the corresponding pixel. So, the fitted testing ISRF for each pixel is not totally the same.

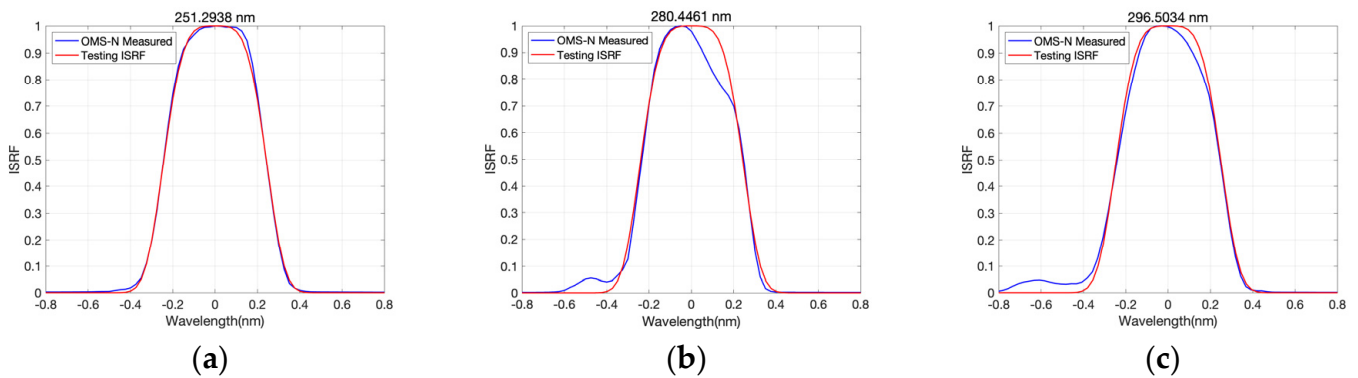


**Figure 18.** An example of the measured ISRF (blue lines) and the testing ISRF (red lines) in the UV1 band. (a) Short wavelength; (b) middle wavelength; (c) long wavelength.

Figure 19a shows the high-resolution TSIS solar spectra, and the simulated irradiance spectra from OMS-N measured the testing ISRF. In Figure 19a, the light blue test line almost completely covers the red analog line. Therefore, the relative irradiance difference between the solar spectra simulated by the two ISRFs was calculated, as shown in Figure 19b, where green, red, and blue lines indicate the relative irradiance difference from short to long wavelengths. It illustrates that the irradiance difference comes from the influence of a large “asymmetric central peak” + “secondary peak” at the middle wavelength, while in the short and long wavelengths, irradiance differences originate from the slight “asymmetric central peak” and the “asymmetric central peak” + “secondary peak”, respectively. The results show that ISRF characterizations in the UV1 band do not introduce any systematic bias in irradiance. The minor “asymmetric central peak” in short UV1 has little influence on simulated irradiance, with an error standard deviation of 0.07%. However, the uncertainty derived from the mixed effect of the “asymmetric central peak” + “secondary peak” at the middle–long wavelength is within  $\pm 2\%$ . Moreover, this influence is significantly amplified for the center of the absorption line, with a maximum greater than 5%. It reveals that the inaccurate ISRF has a great influence on the spectral absorption line center.

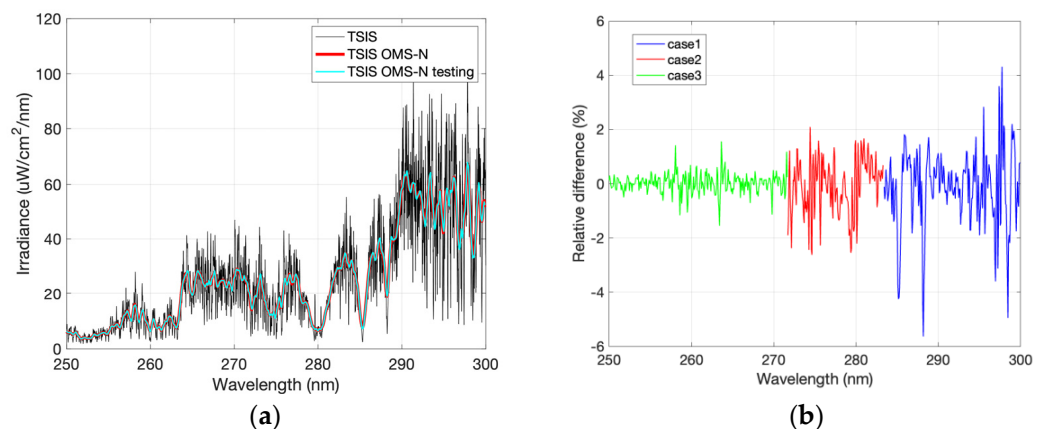


**Figure 19.** The simulated irradiance spectra from OMS-N measured the ISRF (red line) and the testing ISRF (light blue line) and their relative irradiance difference. (a) Simulated irradiance spectra; (b) relative irradiance difference between simulation from the measured ISRF and the testing ISRF.

#### 4.5.3. Impact Analysis: Radiative Transfer Model

The Earth’s radiance is major information used to retrieve atmospheric constituents. To investigate the impact of the OMS-N ISRF on the Earth’s radiance in different surface types, the spectra of the UV1 band at 250–300 nm were modeled using the high spectral resolution radiative transfer model SCIATRAN [26]. The snow and water surfaces were selected to represent surface property with a significant difference, whose albedos were set

to 0.02 and 0.9 in the radiative transfer model (RTM), respectively [27]. The albedo derives from the SCIATRAN surface reflectance database. The simulation results are shown in Figure 20. For 250–300 nm, the simulated spectra are almost the same below 295 nm on snow and water surfaces, which is caused by the continuous absorption of O<sub>3</sub> [28].

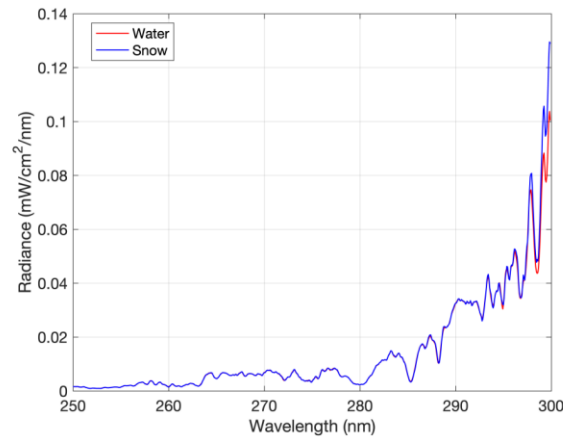


**Figure 20.** The simulated spectra at 250–300 nm on water surface and ice surfaces.

Additionally, we studied the radiance differences triggered by the ISRF “secondary peak” and “asymmetric central peak” on snow and water surfaces. The difference between the measured ISRF and the testing ISRF was discussed separately for snow and water surface types. It can be found in Figure 21 that the consistency of the simulated radiance difference induced by the measured and testing ISRF between snow and water surfaces is within 0.23% in the UV1 band. Consequently, the radiometric uncertainty associated with the “secondary peak” and “asymmetric central peak” of the ISRF in the UV1 band is insensitive to the surface type. The influence of radiance due to ISRF characterizations on surface type is negligible while using Earth observation data.

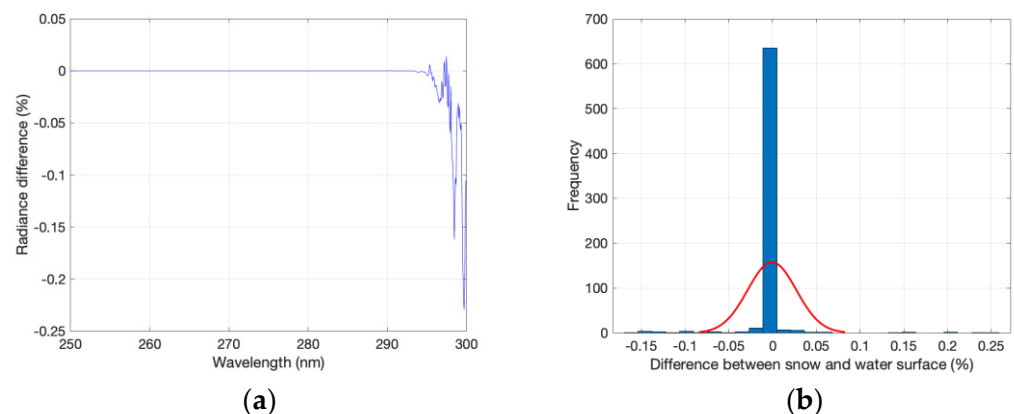


**Figure 21.** The consistency of radiance difference (between the measured ISRF and the testing ISRF) on snow and water surfaces. (a) The radiance difference in the spectral domain; (b) the histogram of the relative radiance difference on snow and water surfaces.

## 5. Conclusions

Accurate laboratory spectral calibration is a primary requirement for data retrieval. The biggest challenge for spectral calibration is determining the ISRF of each pixel. It is very time-consuming work due to the two large array detectors of OMS-N. In this study, an automatically adjustable tunable laser was used to achieve ISRF calibration at most of the spectral coverage of the OMS-N instrument. Based on the data recorded by laser scanning, the ISRF, spectral resolution, and spectral dispersion were measured. After that, spectral accuracy was verified by a standard spectral lamp. In particular, the “asymmetric central

peak” and “secondary peak” of the ISRF in the UV1 band were found; furthermore, the impact analysis was performed. The conclusions are as follows.

1. The spectral resolution and spectral accuracy of OMS-N meet the mission requirements.
2. The characterization of the ISRF shows an “asymmetric central peak” and “secondary peak” in the middle–long wavelength, and a slight “asymmetric central peak” in the short wavelength of the UV1 band. Additionally, the ISRF in the UV1 band is asymmetric, which is more noticeable for nadir rows compared with side rows.
3. ISRF characterizations in the UV1 band do not introduce any radiometric systematic bias. However, if the “asymmetric central peak” and “secondary peak” of the ISRF are ignored, they will bring about an error of  $\pm 2\%$  while simulating observation spectra, with an amplified influence on the center of the absorption line. In data application, the measured ISRF instead of the ISRF fitted by the FWHM should be used, which could avoid the larger errors in the center of the absorption line.

During the commissioning phase of OMS-N, the spectral calibration accuracy and the variation of the ISRF will be further analyzed and verified by solar irradiance observations.

**Author Contributions:** Writing—original draft: Q.W.; calibration experiment: J.M., Y.W., E.S. and Q.W.; conceptualization: N.X., Z.Y., Q.W., X.H., L.S. and L.C.; methodology: Q.W.; data curation and formal analysis: Q.W. and J.M.; writing—review and editing: N.X., P.Z. and Q.W.; supervision: J.L. and F.S. All authors have read and agreed to the published version of the manuscript.

**Funding:** This research was funded by the National Key R&D Program of China, grant numbers 2022YFB3903000 and 2022YFB3903003, and the National Natural Science Foundation of China, grant number U2242212. This research was also funded by the Youth Innovation Team of the “Fengyun Satellite Remote Sensing Product Verification” of the China Meteorological Administration, grant number CMA2023QN12.

**Data Availability Statement:** The data presented in this study are available upon request from the author. The data are not publicly available due to privacy restrictions.

**Acknowledgments:** The authors would like to thank O. Coddington for the high-resolution solar spectra and acknowledge the free use of the SCIATRAN package provided by the ESA and the University of Bremen, respectively.

**Conflicts of Interest:** The authors declare no conflicts of interest.

## References

1. Aminou, D. Copernicus Sentinels 4 and 5 Mission Requirements Traceability Document. [2022-03-02]. 2017. Available online: <https://sentinel.esa.int/documents/247904/0/Copernicus-Sentinels-4-and-5-Mission-Requirements-Traceability-Document.pdf/b15b6786-88cd-4f1d-a67e-a1da70ed595b> (accessed on 4 May 2023).
2. Ingmann, P.; Veihelmann, B.; Langen, J.; Lamarre, D.; Stark, H.; Courrèges-Lacoste, G.B. Requirements for the GMES Atmosphere Service and ESA’s implementation concept: Sentinels-4/-5 and -5p. *Remote Sens. Environ.* **2012**, *120*, 58–69. [[CrossRef](#)]
3. Orfanoz-Chequela, A.; Rozanov, A.; Weber, M.; Arosio, C.; Ladstätter-Weißmayer, A.; Burrows, J.P. Total ozone column from Ozone Mapping and Profiler Suite Nadir Mapper (OMPS-NM) measurements using the broadband weighting function fitting approach (WFFA). *Atmos. Meas. Tech.* **2021**, *14*, 5771–5789. [[CrossRef](#)]
4. Pan, C.; Weng, F.; Flynn, L. Spectral performance and calibration of the Suomi NPP OMPS Nadir/Profiler sensor. *Earth Space Sci.* **2017**, *4*, 737–745. [[CrossRef](#)]
5. Munro, R.; Lang, R.; Klaes, D.; Poli, G.; Retscher, C.; Lindstrot, R.; Huckle, R.; Lacan, A.; Grzegorski, M.; Holdak, A.; et al. The GOME-2 instrument on the Metop series of satellites: Instrument design, calibration, and level 1 data processing—An overview. *Atmos. Meas. Tech.* **2016**, *9*, 1279–1301. [[CrossRef](#)]
6. Zhao, M.; Si, F.; Zhou, H. Pre-Launch Radiometric Characterization of EMI-2 on the GaoFen-5 Series of Satellites. *Remote Sens.* **2021**, *13*, 2843. [[CrossRef](#)]
7. Kleipool, Q.; Ludewig, A.; Babić, L.; Bartstra, R.; Braak, R.; Dierssen, W.; Dewitte, P.J.; Kenter, P.; Landzaat, R.; Leloux, J.; et al. Pre-launch calibration results of the TROPOMI payload onboard the Sentinel-5 Precursor satellite. *Atmos. Meas. Tech.* **2018**, *11*, 6439–6479. [[CrossRef](#)]
8. Platt, U.; Stutz, J. Differential Optical Absorption Spectroscopy (DOAS). In *Air Monitoring by Spectroscopic Techniques*; Sigrist, M.W., Ed.; Chemical Analysis Series; Springer: Berlin/Heidelberg, Germany, 2008; pp. 135–174.

9. Lerot, C.; Van Roozendaal, M.; Lambert, J.C.; Granville, J.; Van Gent, J.; Loyola, D.; Spurr, R. The GODFIT algorithm: A direct fitting approach to improve the accuracy of total ozone measurements from GOME. *Int. J. Remote Sens.* **2010**, *31*, 543–550. [[CrossRef](#)]
10. Lerot, C.; Van Roozendaal, M.; Lambert, J.C.; Granville, J.; Van Gent, J.; Loyola, D.; Spurr, R. Sixteen years of GOME/ERS2 total ozone data: The new direct-fitting GOME Data Processor (GDP) Version 5: I. Algorithm Description. *J. Geophys. Res.* **2012**, *117*, D03305.
11. Tilstra, L.G.; van Soest, G.; Stammes, P. Method for in-flight satellite calibration in the ultraviolet using radiative transfer calculations, with application to Scanning Imaging Absorption Spectrometer for Atmospheric Chartography (SCIAMACHY). *J. Geophys. Res. Atmos.* **2005**, *110*, D18311. [[CrossRef](#)]
12. Mettig, N.; Weber, M.; Rozanov, A.; Arosio, C.; Burrows, J.P.; Veefkind, P.; Thompson, A.M.; Querel, R.; Leblanc, T.; Godin-Beekmann, S.; et al. Ozone profile retrieval from nadir TROPOMI measurements in the UV range. *Atmos. Meas. Tech.* **2021**, *14*, 6057–6082. [[CrossRef](#)]
13. Garane, K.; Koukoulis, M.-E.; Verhoelst, T.; Lerot, C.; Heue, K.P.; Fioletov, V.; Balis, D.; Bais, A.; Bazureau, A.; Dehn, A.; et al. TROPOMI/S5P total ozone column data: Global ground-based validation and consistency with other satellite missions. *Atmos. Meas. Tech.* **2019**, *12*, 5263–5287. [[CrossRef](#)]
14. Hao, N.; Loyola, D.; Van Roozendaal, M.; Lerot, C.; Spurr, R.; Koukoulis, M.; Zyrichidou, I.; Inness, A.; Valks, P.; Zimmer, W.; et al. The operational Near-Real-Time Total Ozone Retrieval Algorithm for GOME-2 on MetOp-A & MetOp-B and perspectives for TROPOMI/S5P, ESA ATMOS. In Proceedings of the Quadrennial Ozone Symposium of the International Ozone Commission (IO3C), Edinburgh, UK, 4–9 September 2016.
15. Jos, H.; Geffen, V.; Roeland, F. Wavelength calibration of spectra measured by the Global Ozone Monitoring Experiment by use of a high-resolution reference spectrum. *Appl. Optics* **2003**, *42*, 2739–2753.
16. Yang, Z.; Zhen, Y.; Yin, Z.; Lin, C.; Bi, Y.; Liu, W.; Wang, Q.; Wang, L.; Gu, S.; Tian, L. Laboratory spectral calibration of the TanSat atmospheric carbon dioxide grating spectrometer. *Geosci. Instrum. Methods Data Syst.* **2018**, *7*, 245–252. [[CrossRef](#)]
17. Smorenburg, K.; Dobber, M.R.; Schenkeveld, E.; Vink, R.; Visser, H. Slit function measurement optical stimulus. In *Sensors, Systems, and Next-Generation Satellites VI*; SPIE: Bellingham, WA, USA, 2003; Volume 4881, pp. 511–520.
18. Day, J.O.; O'Dell, C.W.; Pollock, R.; Bruegge, C.J.; Rider, D.; Crisp, D.; Miller, C.E. Preflight Spectral Calibration of the Orbiting Carbon Observatory. *IEEE Geosci. Remote Sens.* **2011**, *49*, 2793–2801. [[CrossRef](#)]
19. Lee, R.A.M.; O'Dell, C.W.; Wunch, D.; Roehl, C.M.; Osterman, G.B.; Blavier, J.-F.; Rosenberg, R.; Chapsky, L.; Frankenberg, C.; Hunyadi-Lay, S.L.; et al. Preflight Spectral Calibration of the Orbiting Carbon Observatory 2. *IEEE Trans. Geosci. Remote Sens.* **2017**, *55*, 2499–2508. [[CrossRef](#)]
20. Gaiser, S.; Aumann, H.; Strow, L.; Hannon, S.; Weiler, M. In-flight spectral calibration of the atmospheric infrared sounder. *IEEE Trans. Geosci. Remote Sens.* **2003**, *41*, 287–297. [[CrossRef](#)]
21. Sun, K.; Liu, X.; Nowlan, C.R.; Cai, Z.; Chance, K.; Frankenberg, C.; Lee, R.A.M.; Pollock, R.; Rosenberg, R.; Crisp, D. Characterization of the OCO-2 instrument line shape functions using on-orbit solar measurements. *Atmos. Meas. Tech.* **2017**, *10*, 939–953. [[CrossRef](#)]
22. Beirle, S.; Lampel, J.; Lerot, C.; Sihler, H.; Wagner, T. Parameterizing the instrumental spectral response function and its changes by a super-Gaussian and its derivatives. *Atmos. Meas. Tech.* **2021**, *10*, 581–598. [[CrossRef](#)]
23. Robertson, J.G. Quantifying Resolving Power in Astronomical Spectra. *Publ. Astron. Soc. Aust.* **2013**, *30*, e048. [[CrossRef](#)]
24. Yan, C.S.; Chen, Y.W.; Yang, H.M.; Ahokas, E. Optical spectrum analyzers and typical applications in astronomy and remote sensing. *Rev. Sci. Instrum.* **2023**, *94*, 081501. [[CrossRef](#)]
25. Coddington, O.M.; Richard, E.C.; Harber, D.; Pilewskie, P.; Woods, T.N.; Chance, K.; Liu, X.; Sun, K. The TSIS-1 Hybrid Solar Reference Spectrum. *Geophys. Res. Lett.* **2021**, *48*, e2020GL091709. [[CrossRef](#)] [[PubMed](#)]
26. Mei, L.; Rozanov, V.; Rozanov, A.; Burrows, J.P. SCIATRAN software package (V4.6): Update and further development of aerosol, clouds, surface reflectance databases and models. *Geosci. Model Dev.* **2023**, *16*, 1511–1536. [[CrossRef](#)]
27. Wang, Q.; Zhang, P.; Xu, N.; Chen, L.; Wu, R.; Liu, J.; Si, F. An Investigation on Inter-Calibrating EMI/GF-5 with TROPOMI/S5p in Ultraviolet–Visible Spectra. *IEEE Trans. Geosci. Remote Sens.* **2022**, *60*, 1–116. [[CrossRef](#)]
28. Ding, S.; Weng, F. Influences of Physical Processes and Parameters on Simulations of TOA Radiance at UV Wavelengths: Implications for Satellite UV Instrument Validation. *J. Meteor. Res.* **2019**, *33*, 264–375. [[CrossRef](#)]

**Disclaimer/Publisher's Note:** The statements, opinions and data contained in all publications are solely those of the individual author(s) and contributor(s) and not of MDPI and/or the editor(s). MDPI and/or the editor(s) disclaim responsibility for any injury to people or property resulting from any ideas, methods, instructions or products referred to in the content.